energies

MDPI

Article

Airside Thermal Performance of Louvered Fin Flat-Tube Heat Exchangers with Different Redirection Louvers

Arslan Saleem [1] and Man-Hoe Kim [2,*]

[1] School of Engineering, Cardiff University, Queen's Buildings, The Parade, Cardiff CF24 3AA, UK
[2] School of Mechanical Engineering & IEDT, Kyungpook National University, Daegu 41566, Korea
* Correspondence: manhoe.kim@knu.ac.kr; Tel.: +82-53-950-5576; Fax: +82-53-950-6550

Abstract: The performance of heat exchangers is severely limited by airside thermal resistance. The effect of redirection louvers (RLs) on the airside thermal performance of a compact flat-tube louvered fin heat exchanger was investigated. A steady-state 3D numerical analysis was conducted for different fin configurations by varying the number of RLs (N_{RL} = 1, 2, 3, and 5). Conjugate heat transfer analysis was performed at the low Re (50–450) for domestic and transport air-conditioning applications. Geometric parameters such as louver pitch, louver angle, fin pitch, and flow depth were set as 1.7 mm, 27°, 1.2 mm, and 20 mm, respectively. The effective heat transfer fin surface areas of different fin configurations were also kept identical for a comparative analysis. The influence of the RLs on the airside thermal–hydraulic performance was analysed by exploring the local and average Nusselt numbers, pressure drop, Colburn *j* factor, friction factor *f*, performance evaluation criteria (PEC), and flow efficiency of different fin configurations. The numerical results revealed that the asymmetric fin configuration with two RLs (N_{RL} = 2) showed the best heat transfer performance for the entire Re range. It resulted in a 33% higher average Nusselt number, causing a 24% higher pressure drop compared to N_{RL} = 5. At low flow velocities (Re < 75), N_{RL} = 3 showed better PEC; however, at high flow velocities (Re > 75), N_{RL} = 1 outperformed other fin configurations. Finally, it was noted that increasing the number of RLs reduced the amplitude of the wavy-shaped flow formed between the neighbouring louvered fin, consequently deteriorating the flow efficiency.

Keywords: heat exchanger; louver fin; RL; Colburn *j* factor; friction factor

Citation: Saleem, A.; Kim, M.-H. Airside Thermal Performance of Louvered Fin Flat-Tube Heat Exchangers with Different Redirection Louvers. *Energies* **2022**, *15*, 5904. https://doi.org/10.3390/en15165904

Academic Editor: Gianpiero Colangelo

Received: 25 July 2022
Accepted: 12 August 2022
Published: 15 August 2022

1. Introduction

Efficient thermal management systems have been developed with the aim of reducing energy consumption as well as improving thermal performance; in recent years, the compactness and miniaturisation of heat exchangers and radiators has garnered increasing attention. Various state-of-the-art techniques have been used to enhance the thermal performance of heat exchangers. For example, the cooling of automotive engines [1–5], heat sinks using nanofluids [6–13], space heating via heat exchangers [14–18], cooling electronic devices using heat-pipe radiators [19–21], and refrigerant/oil miscibility analysis in refrigeration systems [22,23] have been studied. The compact flat-tube louvered fin heat exchanger has widespread applications in heat pumps, air-conditioning, and refrigeration systems in residential, industrial, and automotive sectors. The flat-tube louvered fin heat exchanger performs better than its counterparts owing to its advantageous features such as compact size, low refrigerant charge, and high pressure sustainability. Airside heat transfer contributes the most to the overall thermal resistance; thus, the overall performance of the heat exchanger is limited. The desire to enhance the airside thermal–hydraulic performance of a microchannel heat exchanger (MCHX) has led to several computational and experimental studies on this topic worldwide.

Kim et al. [24] conducted a comprehensive review of single- and two-phase flows in microchannels and investigated the airside performance under dry, wet, and frosting

conditions based on numerical and experimental studies. Chang and Wang [25] and Chang et al. [26] proposed generalised j and f factor expressions for louvered fin heat exchangers based on a dataset of 91 samples with certainty levels of 89.3% and 83.1%, respectively. Kim and Bullard [27] investigated the airside heat transfer and pressure drop characteristics of 45 heat exchangers with different geometrical fin parameters. Moreover, they developed j and f factor correlations and revealed that, among other geometric parameters, the pressure drop in a heat exchanger also depends on the flow depth. Kim and Cho [28] experimentally studied the airside thermal–hydraulic performance of a flat-tube louver finned heat exchanger at a low Re. Their results reveal that the critical Re is directly related to the louver pitch-to-fin pitch ratio but is unaffected by variations in the louver angle. Kang and Jun [29] investigated the airside thermal–hydraulic performance of 14 heat exchanger geometries for automobile applications based on different louver pitches and louver angles. They reported that the j and f factors for the louvered fin configuration were 2 and 2.6 times those of the plane fin configuration, respectively.

Several numerical studies have aimed to understand the airside flow physics and thermal performance of flat-tube louvered fin heat exchangers. Tafti et al. [30] performed a two-dimensional (2D) computational analysis to investigate the flow transition in a fin array from steady to unsteady state with increasing Re. They reported the initiation of the von Karman vortex street downstream of the exit louver at Re = 400 and the development of free shear layer instabilities at Re = 900. Moreover, they revealed that the instabilities creeped upstream with a further increase in Re. Atkinson et al. [31] conducted a comparative analysis of 2D and three-dimensional (3D) numerical models to analyse the airside flow and heat transfer over the louvered fin arrays in compact heat transfer. The study showed that the 3D models underestimated the heat transfer results compared to the 2D models, and the 3D model predictions were closer to the experimental results. Perrotin and Clodic [32] performed an experimental and numerical investigation and concluded that the 3D numerical analysis yielded significantly more promising results than the 2D numerical analysis. Moreover, they suggested that the offset between the 3D numerical and experimental results could be reduced by accounting for the calculation of the actual fin efficiency.

Multiple experimental and numerical investigations have implemented various techniques to enhance the thermal–hydraulic performance of MCHX. Ryu et al. [33] utilised the Kriging method and a micro-genetic algorithm based on three geometric parameters, namely, the louver pitch, fin pitch and louver angle, to determine the optimal design of a corrugated louvered fin. Li and Wang [34] conducted an experimental analysis to investigate the performance of seven multi-region louver fin models for Re in the range of 400–1600. The study demonstrated a declining trend of the heat transfer coefficient and pressure drop at higher Re, while an opposite trend was observed with an increase in the number of louver regions. Saleem and Kim [35] conducted a parametric study to investigate the airside performance characteristics of 36 fin configurations based on the louver angle, fin pitch, and flow depth for a low Re in the range of 30–500. Subsequently, they investigated the airside thermal–hydraulic performance of different fin configurations by varying the louver pitch for the same range of Re [36]. Jang and Chen [37] reported optimised variable and initial louver angles for nine frontal air velocities corresponding to Re values ranging from 133 to 1199. Liang et al. [38] performed experimental and computational analyses based on 24 automotive heat exchangers. They demonstrated a 9.3% volume reduction in the automotive evaporator while maintaining the same cooling capacity by utilising reduced louvered fin height. Okbaz et al. [39] numerically and experimentally investigated the thermal–hydraulic performance of louvered fin round tube heat exchangers by varying the fin geometry parameters and frontal air velocity. They reported a 10–4.3% higher thermal performance for a louvered fin round tube heat exchanger than for a wavy fin round tube heat exchanger. Ishaque and Kim [40] performed a performance analysis of a residential heat pump system by varying the geometric parameters of the heat exchanger. Later, Ishaque et al. [41] performed a numerical analysis incorporating

the non-uniform frontal air velocity and investigated the seasonal thermal performance of heat pump systems. Tran et al. [42] employed a multi-nozzle structure to augment the heat transfer rate per unit volume of the MCHX. Recently, Tran and Wang [43] performed a numerical study to optimise the airside thermal performance by varying the direction of the fins in the latter half of the fin array and proposed a composite straight and louvered fin configuration. Vaisi et al. [44] performed a one-dimensional transient simulation of fin-and-tube heat exchangers with step-variation of air and water inlet temperatures. In another study, Vaisi et al. [45] conducted experimental and numerical analysis to investigate the geometrical parameters (louver pitch, louver arrangement, and number of louver regions). They reported that the symmetrical arrangement of louvered fins resulted in a 9.3% higher thermal performance. Recently, Moosavi et al. [46] determined the minimum distance of headers through numerical investigation of the geometrical structure of the louvered fins in fin-tube heat exchangers. They reported that the redirection of flow is dependent on the louver angle and distance of the flow redirection location from the inlet edge of the fin.

A literature survey showed that several parametric studies have been conducted to improve the airside thermal–hydraulic performance of louvered fin flat-tube heat exchangers. However, there is still a considerable gap in the knowledge regarding the effect of RLs. In this study, the influence of RLs on the airside thermal–hydraulic performance over a low Re range of 50 to 450 was numerically investigated for residential applications. A 3D conjugate heat transfer analysis was performed by employing different fin configurations and varying the number of RLs. The simulation results were used to identify the flow changes in symmetric and asymmetric fin configurations. In addition, the airside thermal–hydraulic performance characteristics were investigated based on local heat transfer and pressure drop data.

2. Numerical Methodology

2.1. Problem Description and Computational Model

A schematic of the louvered fin and the respective geometric parameters under consideration are shown in Figure 1. Four fin configurations with a varying number of RLs were analysed; the rest of the geometric parameters were constant. Table 1 lists the values of the geometric parameters for different fin configurations, and Figure 2 shows a schematic of different fin configurations. Most of the studies in the literature have modelled the airflow in MCHX as laminar with the assumption of a constant tube wall temperature. Few studies claim that the flow can be assumed to be laminar up to the Re 400, and turbulence starts to appear at higher Re. In this study, conjugate heat transfer was modelled to consider the effects of fin conduction and convection. Moreover, the flow field is treated as laminar since the Re range studied is from 50 to 450. The continuity equation is given by Equation (1), whereas the momentum equation in Cartesian coordinates is given by Equations (2)–(4) for the steady-state incompressible flow-field.

$$\frac{\partial u}{\partial x} + \frac{\partial v}{\partial y} + \frac{\partial w}{\partial z} = 0 \tag{1}$$

$$\rho\left(u\frac{\partial u}{\partial x} + v\frac{\partial u}{\partial y} + w\frac{\partial u}{\partial z}\right) = -\frac{\partial p}{\partial x} + \mu\left(\frac{\partial^2 u}{\partial x^2} + \frac{\partial^2 u}{\partial y^2} + \frac{\partial^2 u}{\partial z^2}\right) \tag{2}$$

$$\rho\left(u\frac{\partial v}{\partial x} + v\frac{\partial v}{\partial y} + w\frac{\partial v}{\partial z}\right) = -\frac{\partial p}{\partial y} + \mu\left(\frac{\partial^2 v}{\partial x^2} + \frac{\partial^2 v}{\partial y^2} + \frac{\partial^2 v}{\partial z^2}\right) \tag{3}$$

$$\rho\left(u\frac{\partial w}{\partial x} + v\frac{\partial w}{\partial y} + w\frac{\partial w}{\partial z}\right) = -\frac{\partial p}{\partial z} + \mu\left(\frac{\partial^2 w}{\partial x^2} + \frac{\partial^2 w}{\partial y^2} + \frac{\partial^2 w}{\partial z^2}\right) \tag{4}$$

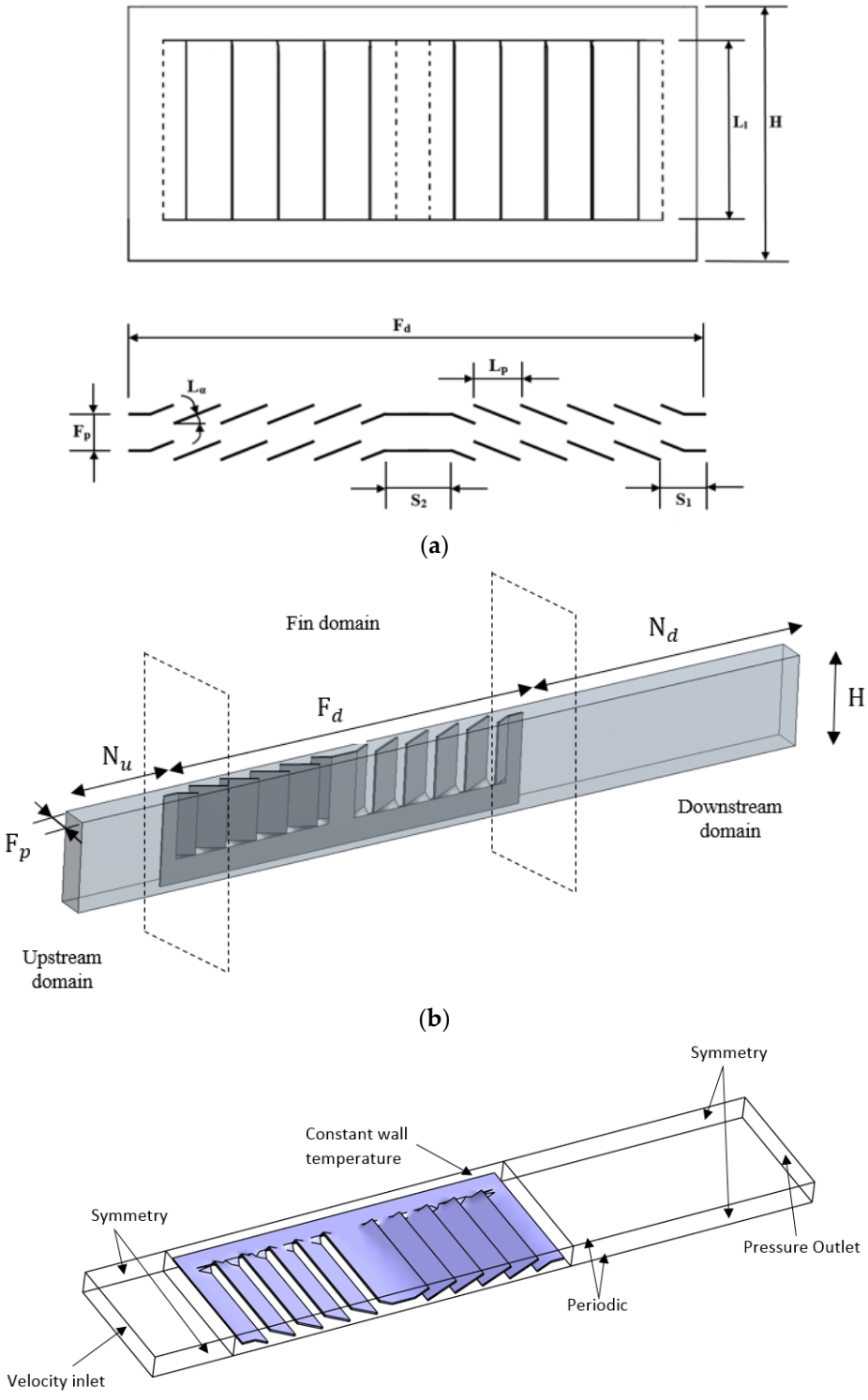

Figure 1. Geometric details, discretization of the computational domain, and imposed boundary conditions. (**a**) Schematic of the louvered fin geometry. (**b**) Discretization of the computational domain. (**c**) Boundary conditions.

Table 1. Geometrical parameters of louvered fin geometry.

Geometric Configuration	Fin Pitch (mm)	Flow Depth (mm)	Louver Angle (deg)	Louver Pitch (mm)	Louver Length (mm)	Fin Height (mm)	Fin Thickness (mm)	Non-Louvered Inlet and Exit Fin Length (mm)	Non-Louvered Redirection Fin Length (mm)	Number of Redirection Louvers
	F_p	F_d	L_α	L_p	L_l	H	δ_f	S_1	S_2	N_{RL}
1	1.2	20	27	1.7	6.4	8.15	0.1	1.0	1.2	1
2	1.2	20	27	1.7	6.4	8.15	0.1	0.8	1.2	2
3	1.2	20	27	1.7	6.4	8.15	0.1	1.2	1.2	3
4	1.2	20	27	1.7	6.4	8.15	0.1	1.5	1.2	5

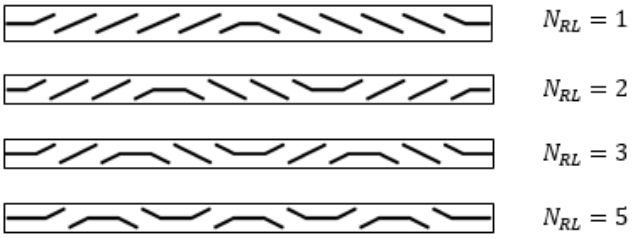

Figure 2. Schematic showing different fin configurations.

The energy equations for the fluid and the solid domains are given by Equations (5) and (6), respectively.

$$u\frac{\partial T}{\partial x} + v\frac{\partial T}{\partial y} + w\frac{\partial T}{\partial z} = \frac{\lambda_f}{\rho_f c_{p_f}}\left(\frac{\partial^2 T}{\partial x^2} + \frac{\partial^2 T}{\partial y^2} + \frac{\partial^2 T}{\partial z^2}\right) \tag{5}$$

$$\lambda_s\left(\frac{\partial^2 T}{\partial x^2} + \frac{\partial^2 T}{\partial y^2} + \frac{\partial^2 T}{\partial z^2}\right) = 0 \tag{6}$$

2.2. Computational Domain and Boundary Conditions

In the present study, the computational domain used to compute the airside heat transfer coefficient consisted of two domains, namely, the fluid domain Ω_f and solid domain Ω_s. The solid domain was enclosed within the fluid domain to depict the solid fin and the airflow around it. The domain Ω_f was segmented into the three fluid domains, upstream and downstream domains, and the fluid domain around the fin as depicted in Figure 1. The upstream and downstream domain lengths were defined as 5 and 15 times the fin pitch value, respectively. The fin domain length was maintained equal to the flow depth of the louvered fin. Only half of the fin was modelled by reducing the width of the computational domain to half of the fin height, to minimize the computational losses. The depth of the computational domain was maintained to be equal to the fin pitch. The boundary conditions imposed on the computational domain are described by Equations (7)–(12).

At the inlet of the flow domain, the velocity inlet boundary condition was used with a constant inlet temperature as follows:

$$u = u_{in};\ v = w = 0;\ T = T_{in}. \tag{7}$$

The periodic boundary condition is applied on both sides of the fluid domain:

$$\frac{\partial u}{\partial z} = \frac{\partial v}{\partial z} = 0 \qquad w = 0 \qquad \frac{\partial T}{\partial z} = 0 \tag{8}$$

The fluid domain outlet face is provided using the pressure outlet boundary condition:

$$\frac{\partial u}{\partial x} = \frac{\partial v}{\partial x} = \frac{\partial w}{\partial x} = \frac{\partial T}{\partial x} = 0 \tag{9}$$

A symmetry boundary condition was defined on the top and bottom faces of the fluid:

$$\frac{\partial u}{\partial y} = \frac{\partial w}{\partial y} = 0 \qquad v = 0 \qquad \frac{\partial T}{\partial y} = 0 \tag{10}$$

A constant temperature is maintained over the tube wall region:

$$u = v = w = 0;\ T = T_w. \tag{11}$$

At the interface of the fluid and solid domain:

$$u = v = w = 0;\ T_s = T_f;\ \lambda_s \frac{\partial T_s}{\partial n} = \lambda_f \frac{\partial T_f}{\partial n}. \tag{12}$$

2.3. Numerical Solution

The finite volume method-based commercial software ANSYS Fluent was used to solve the conservation equations over the entire computational domain. Pressure velocity coupling was achieved by utilising the SIMPLE scheme. A least-square cell-based discretization scheme was employed to simulate the 3D steady-state model. The under-relaxation factors for the pressure, momentum, and energy conservation equations were maintained at 0.3, 0.7, and 1, respectively. The residual values for continuity, momentum, and energy convergence were 1×10^{-6}, 1×10^{-6}, and 1×10^{-7}, respectively.

To reduce interpolation losses, hexahedral elements were used to discretise the entire computational domain, and a conformal mesh interface between the solid and fluid domains was ensured. An O-grid topology was used around the fin louvers to apply clustering near the fin walls. To accurately capture the velocity and temperature profiles over the no-slip boundaries, 15 nodes were placed within the O-grid [47]. The structured grid was generated for all fin configurations using ANSYS ICEMCFD. The four geometric configurations G1 to G4 have 227, 225, 216, and 174 blocks, respectively. The blocking topology of the fin configuration with one RL is shown in Figure 3. Grid orthogonality and quality were ensured to be high for all generated grids. A structured hexahedral grid over the entire computational domain is illustrated in Figure 4.

2.4. Grid Independence Study

Four hexahedral grids of different grid resolutions were generated over the computational domain to conduct a grid independence study. Clustering was applied near the fin walls to accurately capture the velocity and temperature gradients [48,49]. Table 2 lists the particulars of the four different grids and details of the node count over the whole computational domain. The number of nodes upstream $\left(N_{uf}\right)$ and downstream $\left(N_{df}\right)$ of the louvered fin was kept the same for all grid resolutions. Additionally, the node counts within the O-grids (N_o) and along the fin pitch $\left(N_{fp}\right)$ were also maintained unchanged in all grids. The number of nodes along the fin height $\left(N_{fh}\right)$ and flow-depth $\left(N_{fd}\right)$ were varied to generate high-resolution computational grids. Steady-state incompressible flow analysis was performed using different grid sizes at a frontal air velocity of 2 m/s. Figure 5 shows the results of the grid convergence study in terms of the Colburn *j* factor for different grids (G1 to G4). The numerical results reveal that increments in grid spacing from G2 to G4 lead to only 1% accuracy of the *j* factor at the expense of significantly higher computational cost in terms of the solution time and allocation memory. Thus, considering the accuracy and computational cost of the four generated grids, the G2 grid was selected to perform the remaining simulations in the current study.

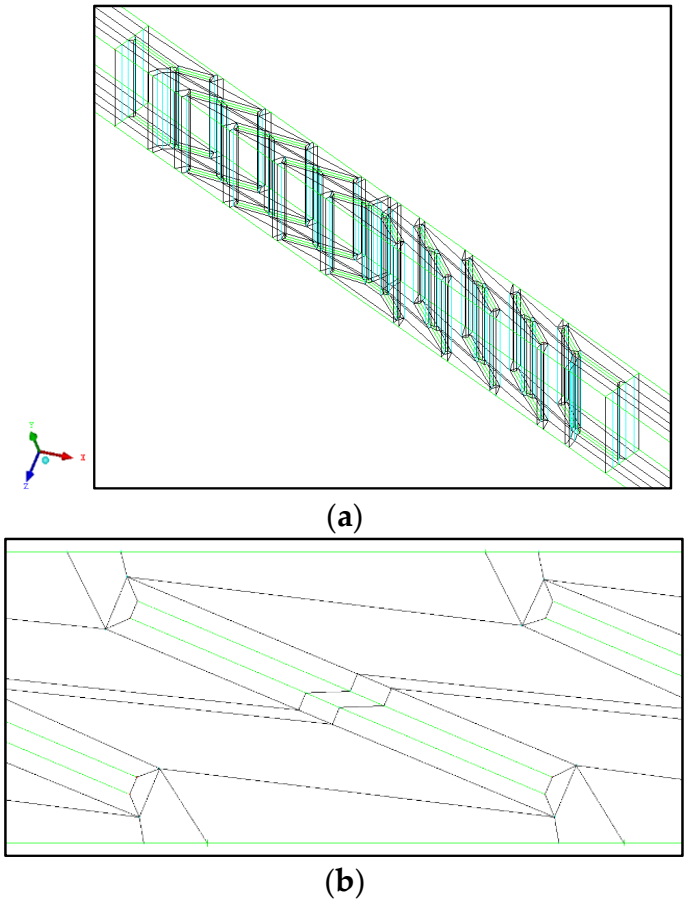

Figure 3. Blocking detail and O-grid topology around the louvered fins. (**a**) Blocking for structured mesh; (**b**) O-grid around louvered fins.

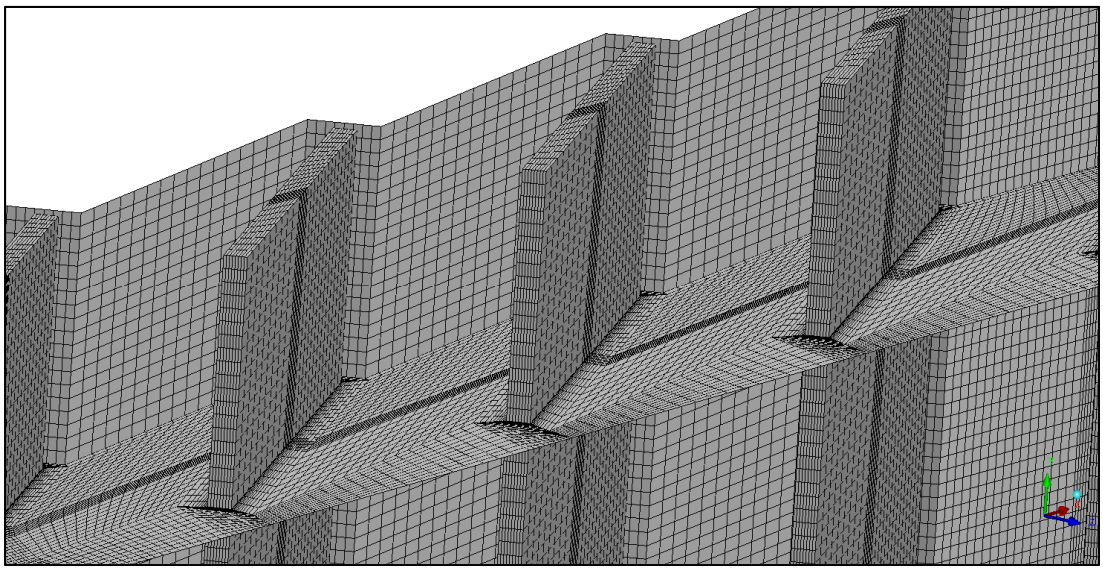

Figure 4. Structured hexahedral mesh over the computational domain.

Table 2. Grid sizing properties.

Grid		G1	G2	G3	G4
Number of nodes upstream	N_{uf}	50	50	50	50
Number of nodes along flow depth	N_{fd}	200	250	300	320
Number of nodes downstream	N_{df}	100	100	100	100
Number of nodes along fin pitch	N_{fp}	50	50	50	50
Number of nodes along fin height	N_{fh}	64	85	100	120
Nodes within the O-grid	N_o	15	15	15	15
Near wall element size	E_{nw} (m)	1.7×10^{-5}	4.1×10^{-6}	2.5×10^{-6}	1×10^{-6}
Total number of elements	N_{te}	1,545,571	2,452,555	3,057,211	3,813,031
Total nodes	N_{tn}	1,452,240	2,323,584	2,904,480	3,630,600

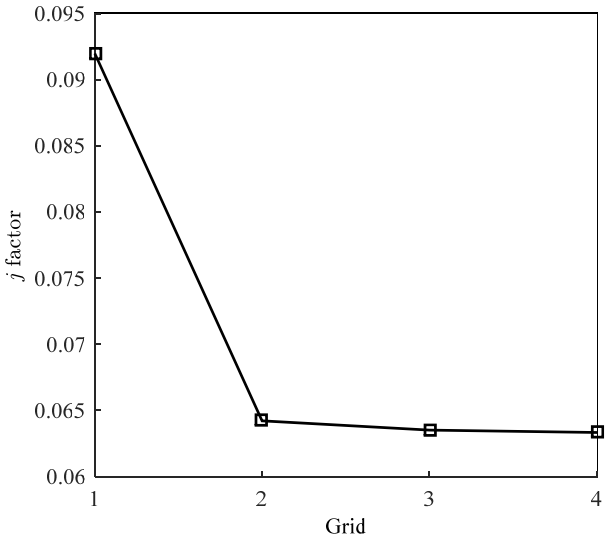

Figure 5. Grid independence study using different grid sizes.

3. Results and Discussion

3.1. Computational Model Validation

The conjugate heat transfer problem was modelled by accounting for conduction through fin walls and convection through the air, to investigate the airside thermal–hydraulic performance. The simulations were performed under thermal conditions such that the air inlet and tube wall temperatures were maintained at 21 and 45 °C, respectively. The constant tube temperature indicates the assumption that the tube wall has an infinite conduction coefficient. Additionally, the water side of the heat exchanger was not simulated to accurately predict the airside heat transfer coefficient. The sensible heat transfer coefficient (h) is expressed as follows:

$$h = \frac{Q}{\eta_o A_o \Delta t_{lm}}, \tag{13}$$

where

$$Q = \dot{m}_a c_p \left(\overline{T}_{ai} - \overline{T}_{ao}\right); \tag{14}$$

$$\eta_o = 1 - \frac{A_f}{A_o}\left(1 - \eta_f\right); \tag{15}$$

$$\eta_f = \frac{\overline{T}_a - \overline{T}_f}{\overline{T}_a - T_w}; \tag{16}$$

$$\Delta t_{lm} = \frac{\overline{T}_{ao} - \overline{T}_{ai}}{\ln\left[\left(T_w - \overline{T}_{ai}\right)/\left(T_w - \overline{T}_{ao}\right)\right]}. \tag{17}$$

The numerical model employed in the present study was validated by comparing the results with those of an experimental study conducted by Shinde and Lin [50]. The geometric parameters of the fin configuration (Sample 2 in the experimental study) were used for validation. The symmetry boundary condition was utilised to model only half of the fin. A comparison of experimental and numerical results is shown in Figure 6, in terms of the Colburn j factor and Fanning friction factor f. The numerical results were in good agreement with the experimental results.

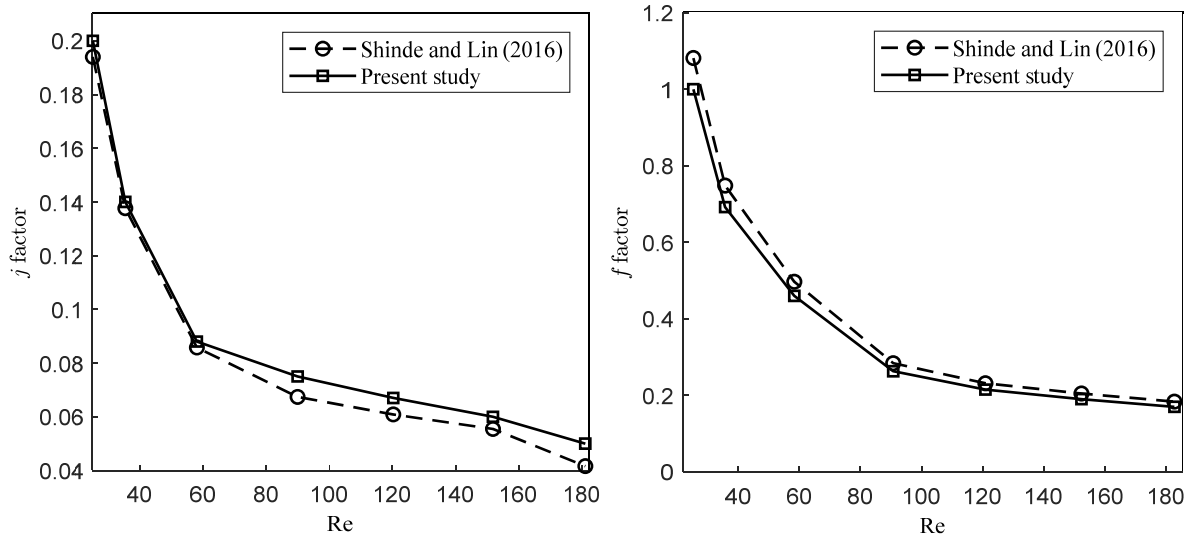

Figure 6. Validation of numerical results with experimental ones from [50].

3.2. Local Heat Transfer Coefficient

Four fin configurations were simulated to investigate the airside local heat transfer coefficients. Commercial software was used to carry out the simulations, and the heat transfer results were reported in terms of the local Nusselt number; however, the commercial software overpredicts the results. This is because the bulk temperature approaches the wall temperature over the wall adjacent nodes owing to the no-slip boundary condition. To resolve this issue, the local airside heat transfer coefficient was calculated by collecting the bulk temperature from the nodes away from the wall. The expressions in Equations (18)–(20) are utilised to estimate the local heat transfer coefficient and local Nusselt number (Nu_{local}) over the top and bottom of the fin at the bisected fin height.

$$T_{fin\ wall} = \frac{\dot{q}_{wall}}{h_{wall}} + T_{wall\ adj} \tag{18}$$

$$h_{local} = \frac{\dot{q}_{wall}}{T_{fin\ wall} - T_{bulk}} \tag{19}$$

$$Nu_{local} = \frac{h_{local} * L_p}{\lambda} \tag{20}$$

The local Nusselt number is plotted over the top and bottom sides of the fin with one RL (shown in Figure 7) at different Re values. The Nusselt number was plotted against the normalised streamwise direction over the fin wall at a fin height of 50%. The leading edges of the louvered fins exhibited the highest local Nusselt numbers. Therefore, a higher heat transfer was observed at the top surface in the first half array of the fin, whereas in the latter half, a higher heat transfer occurred at the bottom surface of the fin. The airside local Nu decreases as the flow passes over the trailing edge of the louver; however, an increase in the local Nu is observed in the case of the RL. This increase in heat transfer can be explained by the flow acceleration over the RL. In the second half of the louvered fin, a higher airside heat transfer coefficient occurs over the bottom side owing to the more pronounced flow than the first half. In addition, the highest local Nusselt number is observed over the leading edge of the louvers in both the first and second halves of the fin at all Re.

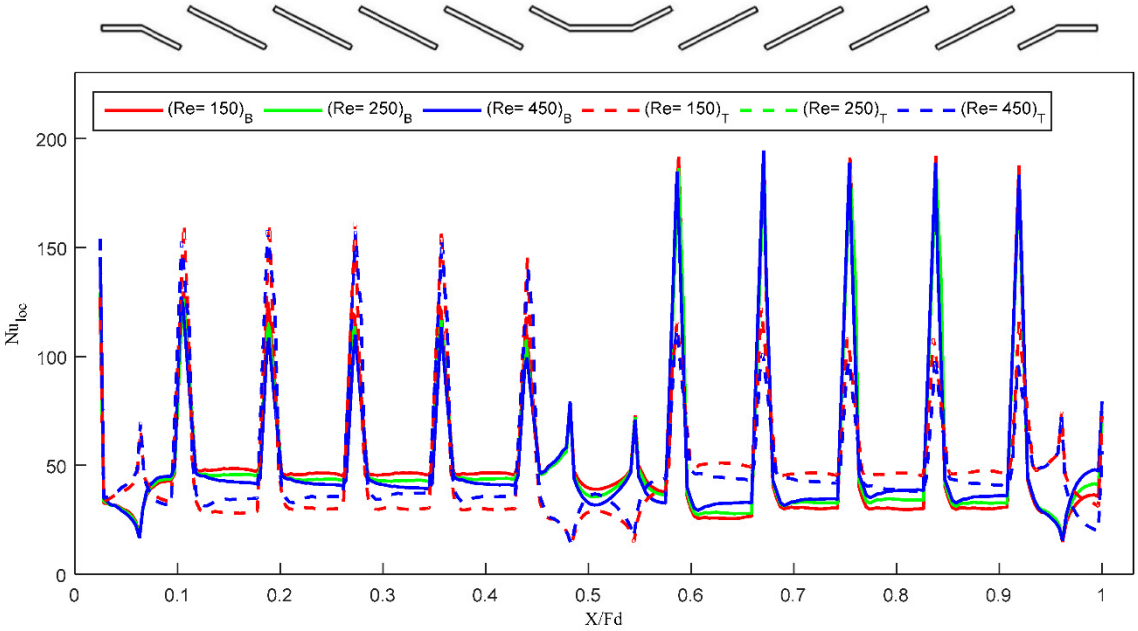

Figure 7. Nu_{local} distribution along the flow depth at Re = 150–450.

The variation in the airside local heat transfer coefficient in different fin configurations was studied for the entire Re range considered in the present study. The trend in the local Nusselt number around the louvered fins for different configurations at a Re of 450 is shown in Figure 8. It is evident from Figure 8a that the local Nusselt number increases downstream of the RL owing to flow acceleration, leading to improved convective heat transfer. This phenomenon was more pronounced in the fin geometry with two RLs, as shown in Figure 8b. The highest local Nusselt number of 291 was observed for the fin configuration $N_{RL} = 2$ at the leading edge of the first louver after the second RL, which can be explained by the boundary layer regeneration phenomenon occurring on the top side louvers, downstream of the second RL. The increment in the airside local heat transfer coefficient diminishes upon further increasing the number of RLs. The increase in the airside local Nusselt number caused by the RL in different fin configurations at a Re of 450 was 36.5, 106.7, 4.6, and 12.9 for $N_{RL} = 1,\ 2,\ 3$, and 5, respectively.

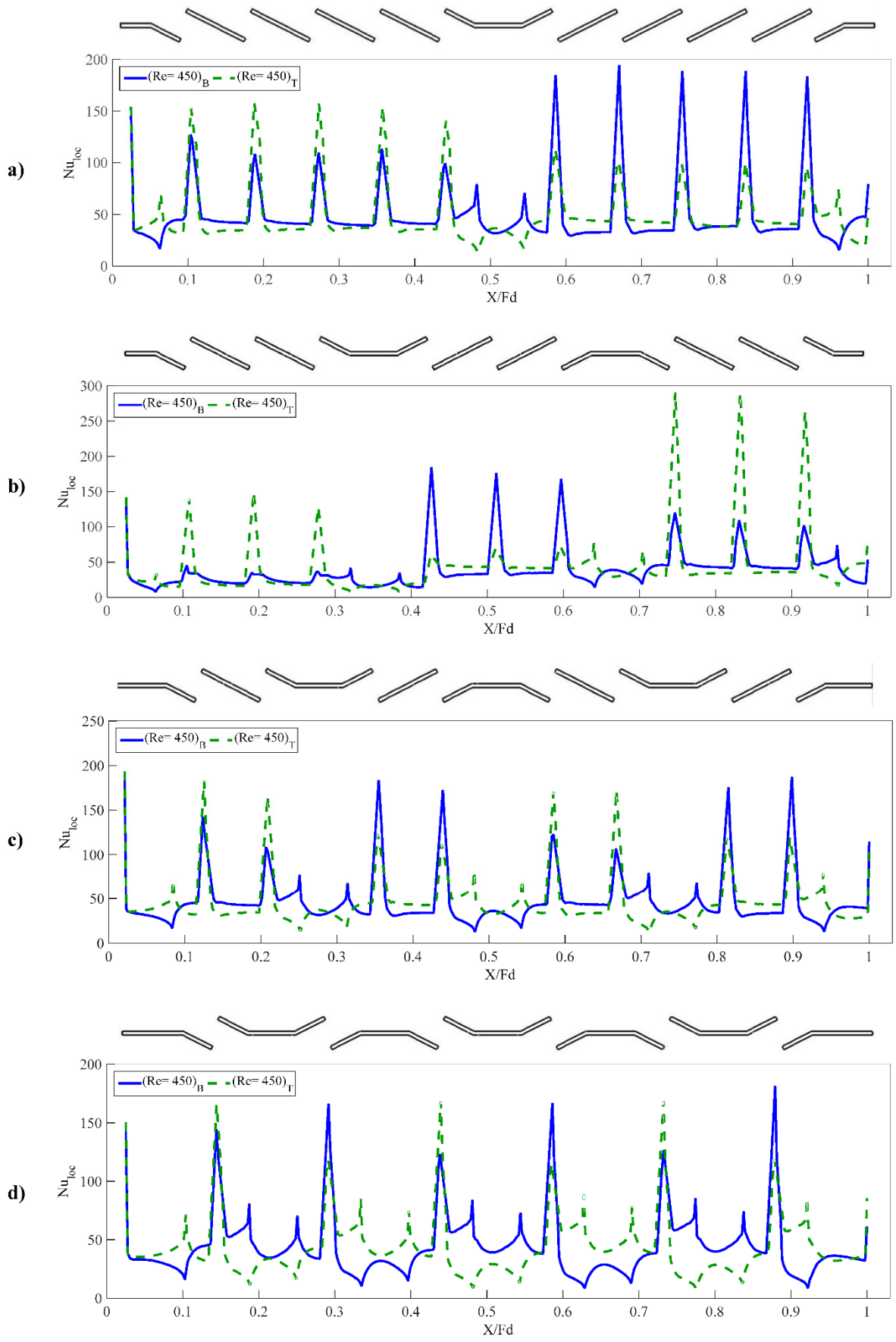

Figure 8. Nu_{local} variation along the flow depth at Re = 450; (**a**) $N_{RL} = 1$, (**b**) $N_{RL} = 2$, (**c**) $N_{RL} = 3$, and (**d**) $N_{RL} = 5$.

The variation in the local airside heat transfer coefficient over the RLs is worth noting. The RL accelerates the flow velocity by redirecting it in the opposite direction. A more pronounced flow velocity was observed over the outer edges, while wakes developed at the inner edges of the RL. Flow acceleration leads to a higher convective heat transfer and a thin thermal boundary layer is observed over the outer side of the RLs. In the case of multiple RLs, each RL accelerates the flow velocity, and the offset between the airside local heat transfer coefficient over the top and bottom of the RL becomes more pronounced. This phenomenon was more prominent in the fin configuration with five RLs, as depicted in Figure 9.

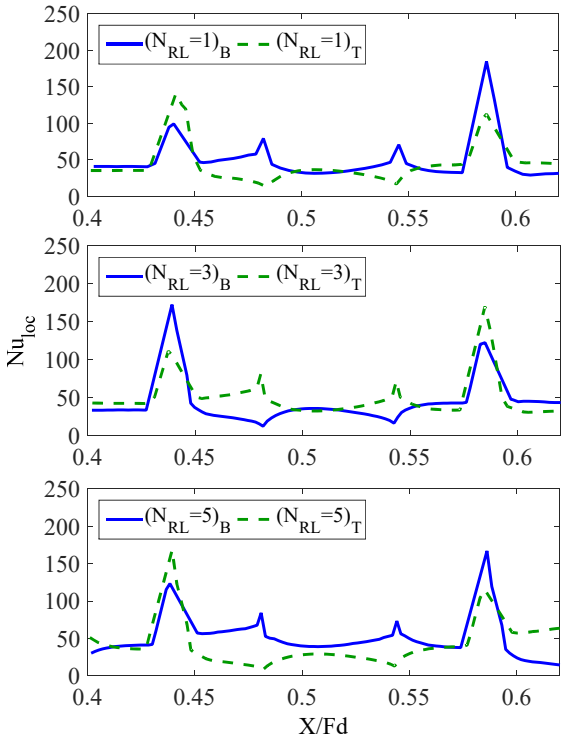

Figure 9. Local Nusselt number variation around the middle RL at Re = 450.

Figure 10 shows the local heat transfer coefficient variation around the first and last louvers. A decline in the local Nusselt number was observed on the inside of the first and last louvers, while an increase was observed on the outside. The heat transfer over the bottom side of the first and last louvers decreased owing to the presence of wakes, whereas it increased on the outer side owing to the flow velocity acceleration. The local Nusselt number curves over the top and bottom of the first and last louvers intercepted each other as the flow moved downstream of the bend. This is because the flow on the bottom side of the first and last louver impinges on the inside of the fin leading to a higher Nusselt number value than that on the other side.

The local airside heat transfer coefficient was calculated by plotting different polylines throughout the fin height. The local Nusselt number was plotted over half and quarter fin height, and it was found that there was no significant variation over the span of the fin height, which is consistent with the previous studies [36]. Figure 11 shows the flow velocity streamlines for different fin configurations at Re = 450. The flow accelerated with an increase in the number of RLs. Moreover, the flow interaction between adjacent fin louvers decreases with increasing RLs. The flow acceleration phenomenon and wakes around the RLs are visible around the outer and inner edges of the RLs. This phenomenon of flow acceleration and wake generation becomes more pronounced with an increasing number of RLs. The temperature distribution within the computational domain at the Re 450 over the bisected fin height is shown in Figure 12. The temperature contours show

that although the air temperature for the fin configuration with five RLs remains relatively lower farther down the flow direction, it heated up quickly upon moving downstream. This can be attributed to the trapped flow between the two adjacent louvered fins. The trapped flow can be more clearly seen in the flow velocity contours where a sinusoidal wavy flow pattern appears between all the adjacent louvered fins of $N_{RL} = 5$. This restricted flow leads to a thick thermal boundary layer around the louvered fins.

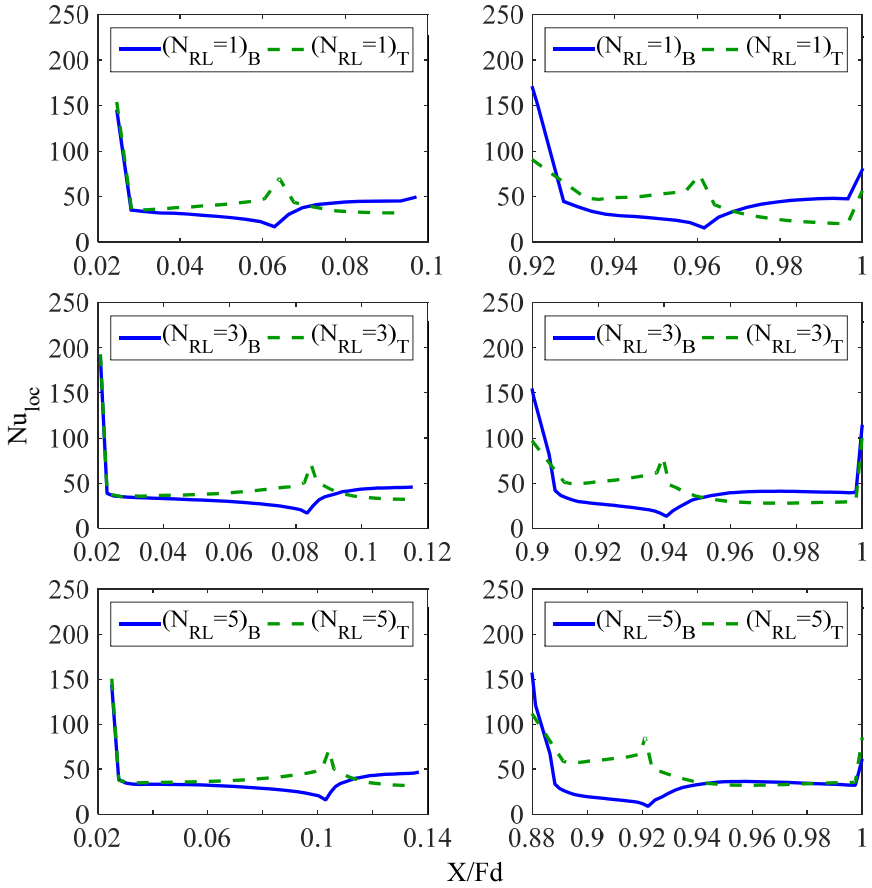

Figure 10. Local Nusselt number around first (**left**) and last (**right**) louvers of different fin configurations at Re = 450.

3.3. Average Heat Transfer Coefficient and Pressure Drop

The average heat transfer and pressure drop were calculated by averaging the local values over the entire fin surface. The average Nusselt number (Nu_{avg}) and pressure drop (ΔP) for the different fin configurations are shown in Figures 13 and 14, respectively. The highest Nu_{avg} and ΔP values were found for the fin configuration with two RLs $(N_{RL} = 2)$. In terms of the heat transfer enhancement, fins with two and three RLs outperformed the baseline configuration with one RL. The improvement in heat transfer due to multiple RLs can be explained using flow physics. The RLs redirect and accelerate the flow, leading to the boundary layer regeneration phenomenon which consequently enhances the heat transfer performance. However, the fin with five RLs underperformed compared to the baseline configuration, indicating that a further increase in the number of RLs, would not positively contribute to the heat transfer enhancement under similar boundary conditions. The fin configuration with $N_{RL} = 5$ and $N_{RL} = 1$ exhibits opposing Nu_{avg} and ΔP trends, which are comprehensible in terms of the local heat transfer coefficient distribution (shown in Figure 8). The higher heat transfer performance of $N_{RL} = 1$ can be explained by the higher number of louvers compared to the $N_{RL} = 5$ configuration, whereas the higher pressure drop for $N_{RL} = 5$ is due to the higher number of RLs. The average Nusselt number and pressure drop increased with the Re. Furthermore, the difference between the

average values of the Nusselt number and the pressure drop became more pronounced with increasing Re. At $Re = 450$, the fin configuration with $N_{RL} = 2$ and $N_{RL} = 3$ showed 24.3% and 16.8% increments in average Nusselt number compared to the baseline fin configuration $N_{RL} = 1$, respectively. The fin configuration with $N_{RL} = 5$ showed a deterioration in heat transfer with an average Nusselt number decrement of 5.9%.

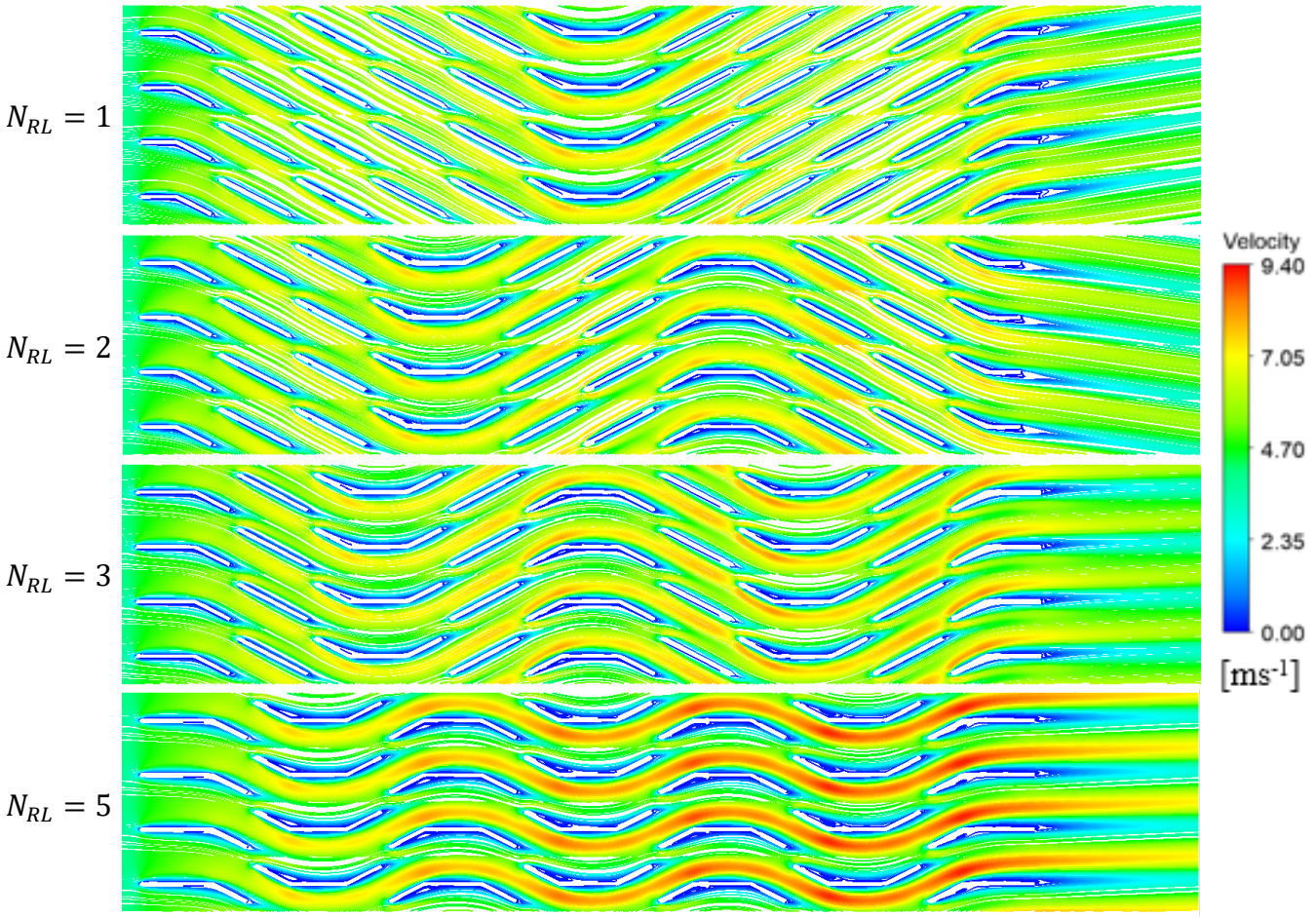

Figure 11. Velocity streamlines of flow around different fin configurations.

At a low Re, the ΔP offset for different fin configurations is minimal; however, it becomes remarkable at a higher Re. The ΔP value for all fin configurations showed a similar trend as a function of Re because the pressure gradient upstream and downstream of the louvers increases with the accelerating flow velocity. The highest pressure drop is observed for fin configuration $N_{RL} = 2$, followed by $N_{RL} = 3$, $N_{RL} = 5$ and $N_{RL} = 1$. The $N_{RL} = 2$ and $N_{RL} = 3$ fin configurations showed better thermal performance at the cost of higher pressure drops of 18–39% and 13–31%, respectively, compared with $N_{RL} = 1$ over the Re range of 50–450.

The heat transfer and pressure drop results were also calculated in terms of Colburn j factor and Fanning friction factor f, using expressions in Equations (21) and (22), respectively.

$$j = \frac{h}{\rho_m U c_p} \mathrm{Pr}^{2/3}; \tag{21}$$

$$f = \frac{2\Delta p}{\rho_m U^2} * \frac{A_c}{A}, \tag{22}$$

where A_c, A, h, U and ρ_m represent the critical area, airside surface area, airside heat transfer coefficient, face air velocity, and mean air density, respectively. The j and f factors

are plotted against the considered Re range for the different fin configurations in Figures 15 and 16, respectively. A decreasing trend is observed for both j and f factors with an increasing Re, which is consistent with the findings of other researchers [32,50]. The j factor curves present a similar trend for different fin configurations where the highest j factor values are observed for $N_{RL} = 2$ followed by $N_{RL} = 3$, $N_{RL} = 1$ and $N_{RL} = 5$. The heat exchanger configuration with $N_{RL} = 2$ exhibits an increment of 11.4–24.3% in the j factor for Re = 50–450. The f factor curves shows a trend similar to the j factor curves; that is, the highest friction factor is observed for $N_{RL} = 2$, followed by $N_{RL} = 3$, $N_{RL} = 1$ and $N_{RL} = 5$. The offset between the f factor curves for the different fin configurations decreases with the increasing Re.

$$PEC = \frac{Nu/Nu_0}{(f/f_0)^{1/3}} \tag{23}$$

$$\eta = \frac{N}{D} \tag{24}$$

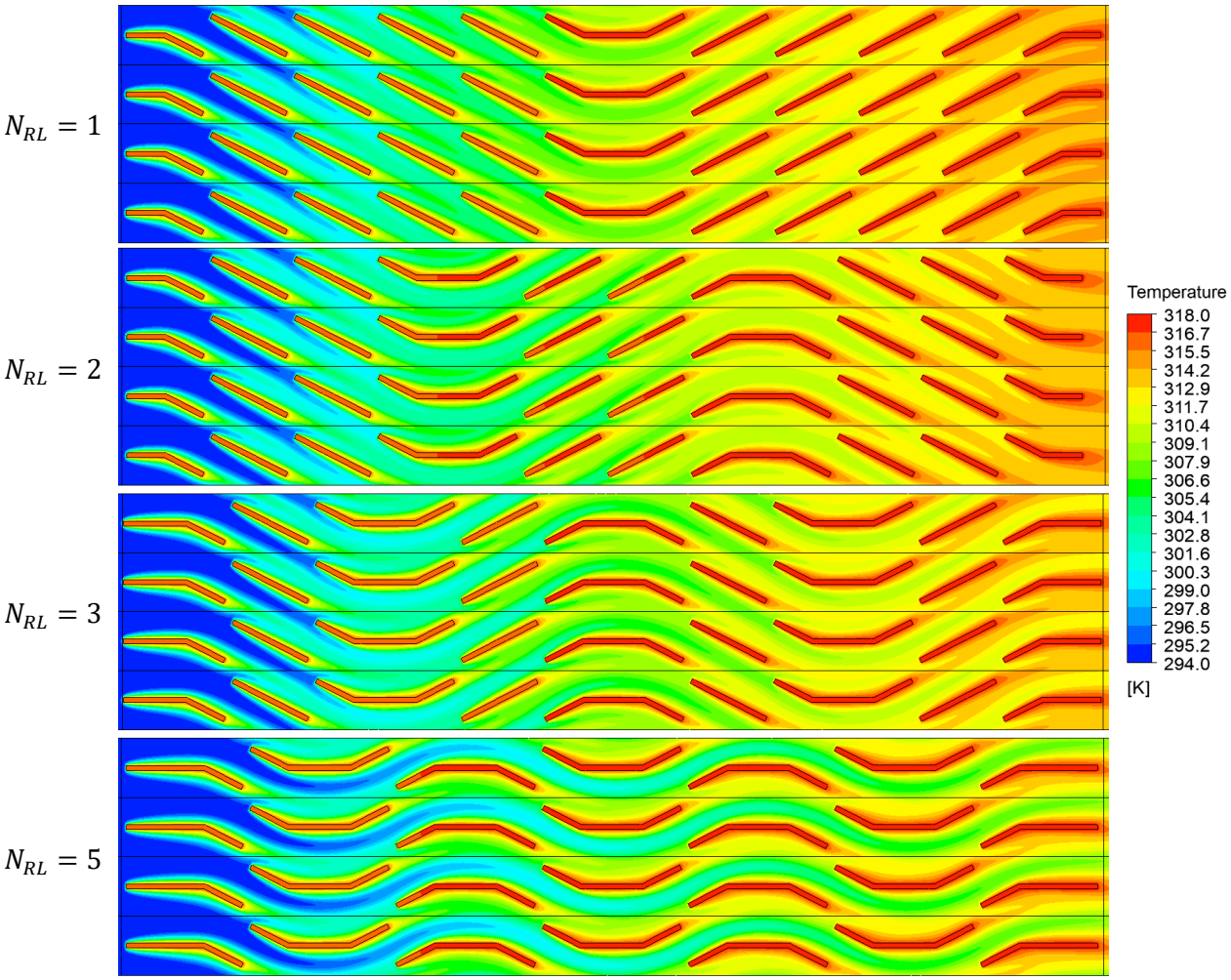

Figure 12. Temperature contours over the bisected plane for different fin configurations.

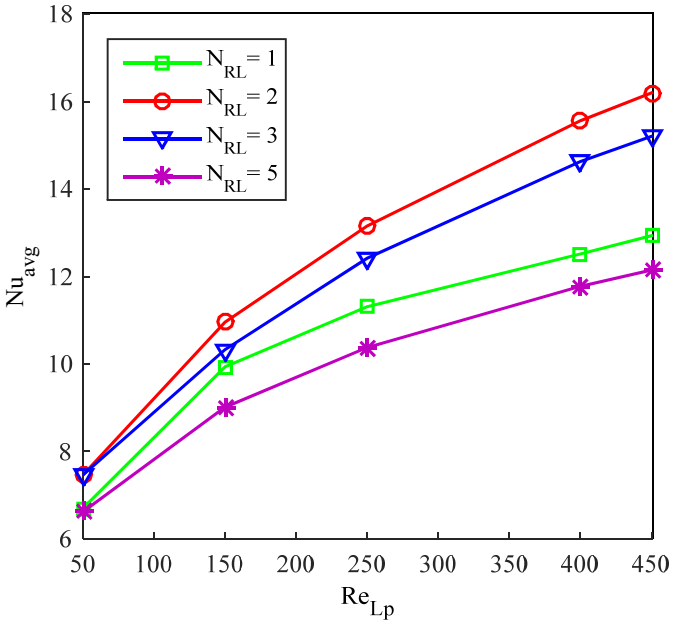

Figure 13. Average Nusselt number variation with Re for different fin geometries.

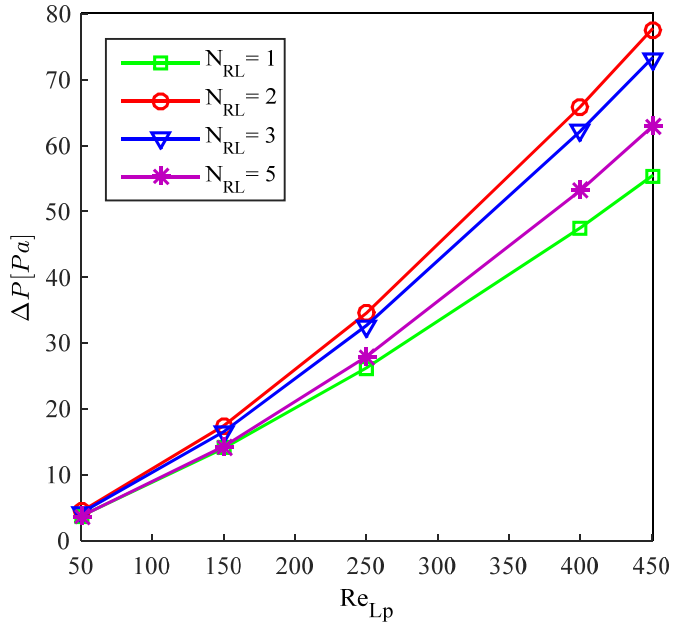

Figure 14. Pressure drop variation with Re for different fin geometries.

Figure 17 presents the heat exchanger performance of different fin configurations over the investigated range of Re. The performance evaluation criteria are calculated using the expression shown in Equation (23). Based on the thermal–hydraulic performance shown by the j and f factor results, the performance evaluation of different fin configurations is performed with respect to $N_{RL} = 5$. At low Re (<75), the fin configuration with $N_{RL} = 3$ shows the best performance, followed by $N_{RL} = 2$ and $N_{RL} = 1$. However, at higher Re (>75), the highest performance is noted in the case of fin configuration with $N_{RL} = 1$ followed by $N_{RL} = 2$ and $N_{RL} = 3$. Therefore, based on performance evaluation criteria, one RL configuration outperforms the other fin configurations. However, since the main purpose of the heat exchanger is to optimize the heat transfer, the fin configuration $N_{RL} = 2$ results in higher thermal performance at the expense of higher pressure drop compared to that with $N_{RL} = 1$. At Re = 450, the percentage increases in the values of Nu_{avg} and ΔP for

$N_{RL} = 2$ compared to those for $N_{RL} = 1$, which are 24.3% and 38.6%, respectively. Hence, a fin configuration with two RLs is recommended for higher heat transfer performance.

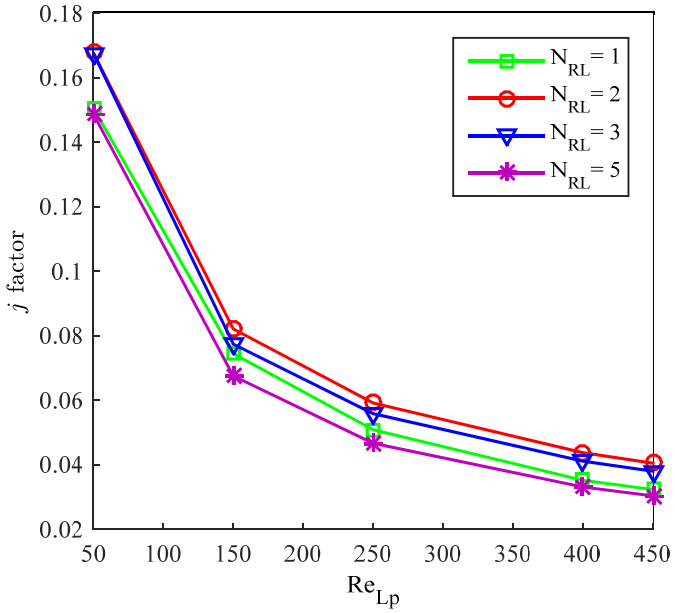

Figure 15. *j* factor variation with Re for different fin geometries.

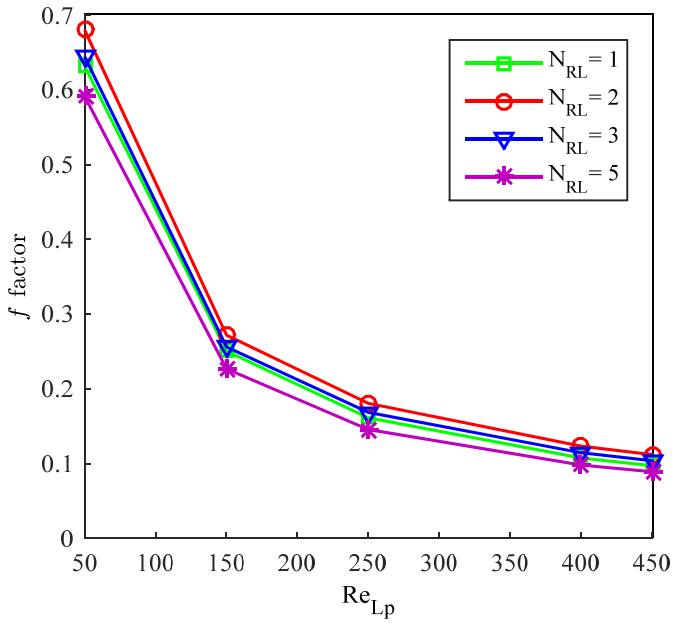

Figure 16. *f* factor variation with Re for different fin geometries.

In addition, the flow efficiency was calculated for different fin configurations over the studied Re range using Equation (24). It was revealed that the variation in Re does not influence the flow efficiency within the investigated Re range. Moreover, the results show that the flow efficiency decreases with an increase in the number of RLs, as shown in Figure 18. The flow efficiency results for different fin configurations were consistent with the performance evaluation criteria. It can be concluded that the performance evaluation criteria are directly dependent on the flow efficiency of the heat exchanger.

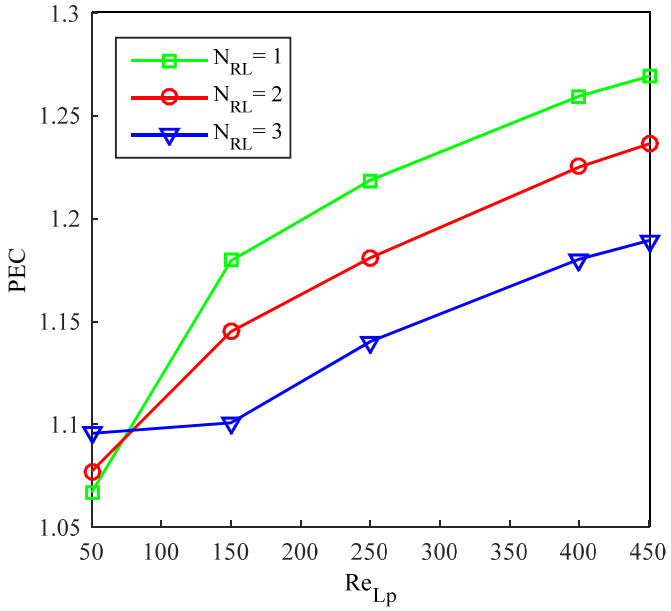

Figure 17. Performance comparison of different geometric configurations.

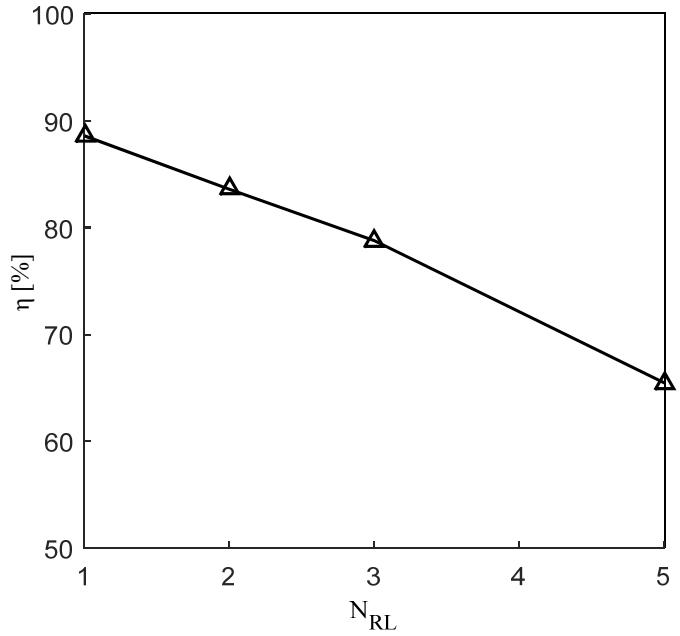

Figure 18. Flow efficiency of different geometric configurations.

4. Conclusions

The aim of this study was to explore the airside thermal–hydraulic performance of a louvered fin flat-tube heat exchanger with varying fin configurations. The thermal performance of different fin configurations with varying RLs was investigated numerically for the Re values ranging from 50 to 450. The results were analysed by studying the local and average airside heat transfer and pressure drop. Moreover, the performance evaluation criteria and flow efficiencies of different fin configurations were investigated. The following key conclusions were drawn from this study:

- The RL accelerates the downstream flow by redirecting it in a different direction, resulting in heat transfer enhancement. The $N_{RL} = 2$ fin configuration exhibits the best thermal performance, with the highest Nu_{local} of 291.

- An increase in the number of RLs reduces the offset between the airside heat transfer coefficient over the top and bottom of the louvers. However, the local heat transfer coefficient offset between the top and bottom surfaces of the RLs increases because of the increased flow velocity, which leads to larger recirculation regions inside the RLs.
- The $N_{RL} = 2$ (asymmetric fin configuration) shows the highest Nu_{avg} increment of 11–24% with the penalty of 18–39% higher ΔP compared to that with $N_{RL} = 1$ (symmetric fin configuration).
- A similar trend in the Colburn j factor and Fanning friction f factor is observed; the highest values of the j and f factor are observed for fin configuration with $N_{RL} = 2$ followed by $N_{RL} = 3$, $N_{RL} = 1$ and $N_{RL} = 5$.
- At a high Re (>75), the fin configuration with $N_{RL} = 1$ showed the highest performance evaluation criteria, followed by $N_{RL} = 2$ and $N_{RL} = 3$ with respect to $N_{RL} = 5$; however, a reverse trend is noted at a low Re (<75).
- The flow efficiency decreases almost linearly with an increase in number of RLs, with the highest flow efficiency of 88.6% for $N_{RL} = 1$. Moreover, the amplitude of the sinusoidal wavy flow occurring between adjacent fins appeared to be inversely proportional to the increasing number of RLs.

Author Contributions: Data curation, A.S.; Formal analysis, A.S.; Funding acquisition, M.-H.K.; Investigation, A.S.; Project administration, M.-H.K.; Software, A.S.; Supervision, M.-H.K.; Writing—original draft, A.S. All authors have read and agreed to the published version of the manuscript.

Funding: This work partly supported by Korea Evaluation Institute of Industrial Technology (KEIT) grant funded by the Korea government (MOTIE) (Project No. 20015917).

Institutional Review Board Statement: Not applicable.

Informed Consent Statement: Not applicable.

Data Availability Statement: Data is contained within the article.

Conflicts of Interest: The authors declare no conflict of interest.

Nomenclature

A	surface area (m^2)	T	temperature (K)
c_p	specific heat at constant pressure $\left(\mathrm{Jkg}^{-1}\mathrm{K}^{-1}\right)$	U	air face velocity (ms^{-1})
D	ideal transverse distance (m)	u, v, w	Cartesian velocity components
F_d	flow depth (m)	x, y, z	Cartesian coordinates
F_h	fin height (m)	Greek symbols	
F_p	fin pitch (m)	η	efficiency
f	Fanning friction factor $(-)$	δ_f	fin thickness
H	fin height (m)	λ	thermal conductivity $\left(\mathrm{Wm}^{-1}\mathrm{K}^{-1}\right)$
h	heat transfer coefficient, $\left(\mathrm{Wm}^{-2}\mathrm{K}^{-1}\right)$	μ	dynamic viscosity (Pa.s)
j	Colburn j-factor $(-)$	ρ	density $\left(\mathrm{Kgm}^{-3}\right)$
L_l	louver length (m)	Superscript	
L_p	louver pitch (m)	$\bar{}$	average
L_α	louver angle $(^\circ)$	Subscripts	
$\dot{m}$	mass flow rate $\left(\mathrm{kgs}^{-1}\right)$	a	air
N	actual transverse distance (m)	d	downstream
N_{RL}	number of RLs	i	inlet
Nu	Nusselt number	B	bottom
p	pressure (Pa)	T	top
Pr	Prandtl number	s	solid
Q	heat transfer rate (W)	f	fin/fluid

$\dot{q}$	heat flux (W/m^2)	m	mean
Re	Re	w	wall
S_1	non-louvered inlet and exit fin length (m)	o	outlet/overall
S_2	non-louvered redirection fin length (m)	u	upstream

References

1. Abbas, F.; Ali, H.M.; Shah, T.R.; Babar, H.; Janjua, M.M.; Sajjad, U.; Amer, M. Nanofluid: Potential evaluation in automotive radiator. *J. Mol. Liq.* **2020**, *297*, 112014. [CrossRef]
2. Ahmadi, M.H.; Ghazvini, M.; Maddah, H.; Kahani, M.; Pourfarhang, S.; Pourfarhang, A.; Heris, S.Z. Prediction of the pressure drop for CuO/(Ethylene glycol-water) nanofluid flows in the car radiator by means of Artificial Neural Networks analysis integrated with genetic algorithm. *Phys. A Stat. Mech. Its Appl.* **2020**, *546*, 124008. [CrossRef]
3. Said, Z.; El Haj Assad, M.; Hachicha, A.A.; Bellos, E.; Abdelkareem, M.A.; Alazaizeh, D.Z.; Yousef, B.A.A. Enhancing the performance of automotive radiators using nanofluids. *Renew. Sustain. Energy Rev.* **2019**, *112*, 183–194. [CrossRef]
4. Greco, A.; Gundabattini, E.; Solomon, D.G.; Rassiah, R.S.; Masselli, C. A Review on Geothermal Renewable Energy Systems for Eco-Friendly Air-Conditioning. *Energies* **2022**, *15*, 5519. [CrossRef]
5. Cristescu, N.D.; Craciun, E.-M.; Soós, E. *Mechanics of Elastic Composites*; Chapman & Hall/CRC Press: Boca Raton, FL, USA, 2003; ISBN 1584884428.
6. Ambreen, T.; Saleem, A.; Park, C.W. Analysis of hydro-thermal and entropy generation characteristics of nanofluid in an aluminium foam heat sink by employing Darcy-Forchheimer-Brinkman model coupled with multiphase Eulerian model. *Appl. Therm. Eng.* **2020**, *173I*, 115231. [CrossRef]
7. Ambreen, T.; Saleem, A.; Ali, H.M.; Shehzad, S.A.; Park, C.W. Performance analysis of hybrid nanofluid in a heat sink equipped with sharp and streamlined micro pin-fins. *Powder Technol.* **2019**, *355*, 552–563. [CrossRef]
8. Ambreen, T.; Saleem, A.; Park, C.W. Numerical analysis of the heat transfer and fluid flow characteristics of a nanofluid-cooled micropin-fin heat sink using the Eulerian-Lagrangian approach. *Powder Technol.* **2019**, *345*, 509–520. [CrossRef]
9. Ambreen, T.; Saleem, A.; Park, C.W. Pin-fin shape-dependent heat transfer and fluid flow characteristics of water- and nanofluid-cooled micropin-fin heat sinks: Square, circular and triangular fin cross-sections. *Appl. Therm. Eng.* **2019**, *158*, 113781. [CrossRef]
10. Ambreen, T.; Saleem, A.; Tanveer, M.; Anirudh, K.; Shehzad, A.; Woo, C. Irreversibility and hydrothermal analysis of the MWCNTs/GNPs-based nanofluids for electronics cooling applications of the pin-fin heat sinks: Multiphase Eulerian-Lagrangian modeling. *Case Stud. Therm. Eng.* **2022**, *31*, 101806. [CrossRef]
11. Ambreen, T.; Saleem, A.; Park, C.W. Thermal efficiency of eco-friendly MXene based nanofluid for performance enhancement of a pin-fin heat sink: Experimental and numerical analyses. *Int. J. Heat Mass Transf.* **2022**, *186*, 122451. [CrossRef]
12. Ambreen, T.; Saleem, A.; Park, C.W. Homogeneous and multiphase analysis of nanofluids containing nonspherical mwcnt and gnp nanoparticles considering the influence of interfacial layering. *Nanomaterials* **2021**, *11*, 277. [CrossRef] [PubMed]
13. Shehzad, S.A.; Sheikholeslami, M.; Ambreen, T.; Saleem, A.; Shafee, A. Numerically simulated behavior of radiative Fe_3O_4 and multi-walled carbon nanotube hybrid nanoparticle flow in presence of Lorentz force. *Appl. Math. Mech. (Engl. Ed.)* **2021**, *42*, 347–356. [CrossRef]
14. Calisir, T.; Yazar, H.O.; Baskaya, S. Thermal performance of PCCP panel radiators for different convector dimensions—An experimental and numerical study. *Int. J. Therm. Sci.* **2019**, *137*, 375–387. [CrossRef]
15. Ganesh, G.A.; Sinha, S.L.; Verma, T.N. Numerical simulation for optimization of the indoor environment of an occupied office building using double-panel and ventilation radiator. *J. Build. Eng.* **2020**, *29*, 101139. [CrossRef]
16. Ploskić, A.; Wang, Q.; Sadrizadeh, S. A holistic performance evaluation of ventilation radiators—An assessment according to EN 442-2 using numerical simulations. *J. Build. Eng.* **2019**, *25*, 100818. [CrossRef]
17. Rahmati, A.R.; Gheibi, A. Experimental and numerical analysis of a modified hot water radiator with improved performance. *Int. J. Therm. Sci.* **2020**, *149*, 106175. [CrossRef]
18. Shao, S.; Zhang, H.; Jiang, L.; You, S.; Zheng, W. Numerical investigation and thermal analysis of a refrigerant-heated radiator heating system coupled with air source heat pump. *Energy Procedia* **2019**, *158*, 2158–2163. [CrossRef]
19. Peng, L.; Liu, D.; Cheng, H. Design and fabrication of the ultrathin metallic film based infrared selective radiator. *Sol. Energy Mater. Sol. Cells* **2019**, *193*, 7–12. [CrossRef]
20. Shenming, X.; Ran, Y.; Limei, S.; Yupeng, W.; Junlong, X.; Huanxin, C. The experimental study of a novel metal foam heat pipe radiator. *Energy Procedia* **2019**, *158*, 5439–5444. [CrossRef]
21. Xiahou, G.; Zhang, J.; Ma, R.; Liu, Y. Novel heat pipe radiator for vertical CPU cooling and its experimental study. *Int. J. Heat Mass Transf.* **2019**, *130*, 912–922. [CrossRef]
22. Saleem, A.; Kim, M.; Saleem, A.; Kim, M. Miscibility analysis of refrigerant of R-404A with synthetic oil. In Proceedings of the Society of Air-Conditioning and Refrigerating Engineers of Korea, Jeju, Korea, 18–21 May 2018; Volume 65, pp. 64–65.
23. Saleem, A.; Kim, M.-H. Miscibility analysis of polyol-ester based oil SW32 with R404A and low-GWP refrigerant R452A. *Int. J. Refrig.* **2021**, *129*, 22–31. [CrossRef]
24. Kim, M.H.; Lee, S.Y.; Mehendale, S.S.; Webb, R.L. *Microchannel Heat Exchanger Design for Evaporator and Condenser Applications*; Academic Press: Chicago, IL, USA, 2003; Volume 37, ISBN 8242869820.

25. Chang, Y.-J.; Wang, C.-C. A generalized heat transfer correlation for Iouver fin geometry. *Int. J. Heat Mass Transf.* **1997**, *40*, 533–544. [CrossRef]
26. Chang, Y.-J.; Hsu, K.-C.; Lin, Y.-T.; Wang, C.-C. A generalized friction correlation for louver fin geometry. *Int. J. Heat Mass Transf.* **2000**, *43*, 2237–2243. [CrossRef]
27. Kim, M.; Bullard, C.W. Air-side thermal hydraulic performance of multi-louvered fin aluminum heat exchangers. *Int. J. Refrig.* **2002**, *25*, 924–934. [CrossRef]
28. Kim, N.H.; Cho, J.P. Air-side performance of louver-finned flat aluminum heat exchangers at a low velocity region. *Heat Mass Transf. Stoffuebertragung* **2008**, *44*, 1127–1139. [CrossRef]
29. Chan Kang, H.; Jun, G.W. Heat transfer and flow resistance characteristics of louver fin geometry for automobile applications. *J. Heat Transfer* **2011**, *133*, 1–6. [CrossRef]
30. Tafti, D.K.; Wang, G.; Lin, W. Flow transition in a multilouvered fin array. *Int. J. Heat Mass Transf.* **2000**, *43*, 901–919. [CrossRef]
31. Atkinson, K.N.; Drakulic, R.; Heikal, M.R.; Cowell, T.A. Two- and three-dimensional numerical models of flow and heat transfer over louvred fin arrays in compact heat exchangers. *Int. J. Heat Mass Transf.* **1998**, *41*, 4063–4080. [CrossRef]
32. Perrotin, T.; Clodic, D. Thermal-hydraulic CFD study in louvered fin-and-flat-tube heat exchangers. *Int. J. Refrig.* **2004**, *27*, 422–432. [CrossRef]
33. Ryu, K.; Yook, S.-J.; Lee, K. Optimal design of a corrugated louvered fin. *Appl. Therm. Eng.* **2014**, *68*, 76–79. [CrossRef]
34. Li, W.; Wang, X. Heat transfer and pressure drop correlations for compact heat exchangers with multi-region louver fins. *Int. J. Heat Mass Transf.* **2010**, *53*, 2955–2962. [CrossRef]
35. Saleem, A.; Kim, M.H. CFD analysis on the air-side thermal-hydraulic performance of multi-louvered fin heat exchangers at low Reynolds numbers. *Energies* **2017**, *10*, 823. [CrossRef]
36. Saleem, A.; Kim, M.H. Air-side thermal hydraulic performance of microchannel heat exchangers with different fin configurations. *Appl. Therm. Eng.* **2017**, *125*, 780–789. [CrossRef]
37. Jang, J.-Y.; Chen, C.-C. Optimization of louvered-fin heat exchanger with variable louver angles. *Appl. Therm. Eng.* **2015**, *91*, 138–150. [CrossRef]
38. Liang, Y.; Liu, C.; Li, C.; Chen, J. Experimental and simulation study on the air side thermal hydraulic performance of automotive heat exchangers. *Appl. Therm. Eng.* **2015**, *87*, 305–315. [CrossRef]
39. Okbaz, A.; Pınarbaşı, A.; Olcay, A.B.; Hilmi Aksoy, M. An experimental, computational and flow visualization study on the air-side thermal and hydraulic performance of louvered fin and round tube heat exchangers. *Int. J. Heat Mass Transf.* **2018**, *121*, 153–169. [CrossRef]
40. Ishaque, S.; Kim, M.H. Seasonal performance investigation for residential heat pump system with different outdoor heat exchanger designs. *Energies* **2019**, *12*, 4714. [CrossRef]
41. Ishaque, S.; Siddiqui, M.I.H.; Kim, M.H. Effect of heat exchanger design on seasonal performance of heat pump systems. *Int. J. Heat Mass Transf.* **2020**, *151*, 119404. [CrossRef]
42. Tran, N.; Chang, Y.J.; Teng, J.T.; Greif, R. Enhancement heat transfer rate per unit volume of microchannel heat exchanger by using a novel multi-nozzle structure on cool side. *Int. J. Heat Mass Transf.* **2017**, *109*, 1031–1043. [CrossRef]
43. Tran, N.; Wang, C.C. Optimization of the airside thermal performance of mini-channel-flat-tube radiators by using composite straight-and-louvered fins. *Int. J. Heat Mass Transf.* **2020**, *250*, 1280–1291. [CrossRef]
44. Vaisi, A.; Talebi, S.; Esmaeilpour, M. Transient behavior simulation of fin-and-tube heat exchangers for the variation of the inlet temperatures of both fluids. *Int. Commun. Heat Mass Transf.* **2011**, *38*, 951–957. [CrossRef]
45. Vaisi, A.; Esmaeilpour, M.; Taherian, H. Experimental investigation of geometry effects on the performance of a compact louvered heat exchanger. *Appl. Therm. Eng.* **2011**, *31*, 3337–3346. [CrossRef]
46. Moosavi, R.; Vaisi, A.; Javaherdeh, K. Investigation of the geometrical structure of louvered fins in fin-tube heat exchangers for determining the minimum distance of the headers. *J. Mech. Sci. Technol.* **2021**, *35*, 1721–1731. [CrossRef]
47. Saleem, A.; Kim, M.H. Performance of buoyant shell horizontal axis wind turbine under fluctuating yaw angles. *Energy* **2019**, *169*, 79–91. [CrossRef]
48. Saleem, A.; Kim, M.H. Effect of rotor tip clearance on the aerodynamic performance of an aerofoil-based ducted wind turbine. *Energy Convers. Manag.* **2019**, *201*, 112186. [CrossRef]
49. Saleem, A.; Kim, M.H. Aerodynamic performance optimization of an airfoil-based airborne wind turbine using genetic algorithm. *Energy* **2020**, *203*, 117841. [CrossRef]
50. Shinde, P.; Lin, C.-X. A heat transfer and friction factor correlation for low air-side Reynolds number applications of compact heat exchangers (1535-RP). *Sci. Technol. Built Environ.* **2016**, *23*, 192–210. [CrossRef]